An efficient ultrathin PtFeNi Nanowire/Ionic liquid conjugate electrocatalyst

Chunji Li[a,1], Bolong Huang[b,1], Mingchuan Luo[a,1], Yingnan Qin[c], Yingjun Sun[c], Yingjie Li[a], Yong Yang[a], Dong Wu[a], Menggang Li[d], Shaojun Guo[a,e,f,*]

[a] Department of Materials Science & Engineering, College of Engineering, Peking University, Beijing, 100871, China
[b] Department of Applied Biology and Chemical Technology, The Hong Kong Polytechnic University, Hung Hom, Kowloon, 999077, Hong Kong SAR, China
[c] College of Chemistry and Molecular Engineering, Qingdao University of Science and Technology, Qingdao, 266042, China
[d] MIIT Key Laboratory of Critical Materials Technology for New Energy Conversion and Storage, School of Chemistry and Chemical Engineering, Harbin Institute of Technology, Harbin, Heilongjiang, 150001, China
[e] BIC-ESAT, College of Engineering, Peking University, Beijing, 100871, China
[f] Department of Energy and Resources Engineering, College of Engineering, Peking University, Beijing, 100871, China

ABSTRACT

Boosting the rate of oxygen reduction reaction (ORR) on Pt surface is essential to the commercialization of proton exchange membrane fuel cells (PEMFCs), which has thus stimulated tremendous efforts in pursuing the optimized oxygen adsorption strength and maximizing the Pt utilization regarding the composition, architecture and surface geometry. Further activity enhancement necessitates strategies other than solely inner/surface tuning of metallic nanocrystals, which *yet* remains scarce. Applying ultrathin PtFeNi trimetallic nanowires (NWs) as the model catalyst, we herein demonstrate the PtFeNi/ionic liquid (IL) conjugate system can greatly boost the ORR rate on Pt surface. The IL conjugated ultrathin PtFeNi NWs (IL/PtFeNi NWs) achieves an impressive mass activity of 2.83 A mg_{Pt}^{-1}, which is 1.72 and 15.5 times higher than the PtFeNi NWs and benchmark Pt/C, respectively. Furthermore, the IL conjugation also improved the durability during the accelerated stability tests when compared to the non-conjugated counterpart. The combination of experimental characterizations and theoretical calculations reveal that the enhanced catalytic performance derives from the IL-induced flexible electronic layer for even modification of the surface activity. The ultrathin IL/PtFeNi interface NWs also show the remarkable performances towards the electro-oxidation of methanol and the H_2O_2 detection. The present interfacial engineering strategy offers a new opportunity to realize further electrocatalytic activity enhancements for future renewable energy applications.

1. Introduction

Due to the high energy density and negligible environmental impact, proton exchange membrane fuel cells (PEMFCs) is considered as the ideal alternative energy-supplying device to conventional internal combustion engine for automobile applications [1–3]. However, the intrinsically sluggish kinetics of oxygen reduction reaction (ORR), occurring at the cathode of PEMFCs, has greatly hindered the wide-adoption of this technology [4–6]. Even using the most active element Pt as the catalyst, the considerably high overpotential (more than 0.4 V) still exists during the operation of PEMFCs, thus resulting in much lower operational efficiency than the thermodynamic prediction [7,8]. Furthermore, the high cost and low abundance of Pt rouse extra

challenges for the commercialization of this promising technology [9]. To address these challenges, it is highly demanded to develop low-Pt loading catalyst with satisfactorily high ORR activity.

The past decade has witnessed tremendous progress both theoretically and experimentally in decreasing the Pt usage while simultaneously promoting the ORR activity [7,10–12]. Two central topics associated with these progress are maximizing the atomic utilization of Pt and optimizing the Pt-O binding strength [13]. Benefiting from the advances of nanotechnology, orders of magnitude enhancement in mass activity (ORR activity in terms of Pt mass) over the benchmark Pt/C has been achieved by rationally tuning the composition, morphology, architecture and surface coordination of Pt-based nanocrystals [14–19]. Especially, ultrathin Pt-based nanowires (NWs) with diameter of only a

---

few atomic layers have attracted substantial interests due to their high fraction of surface atoms, compressive surface strain and strong quantum confinement [20,21]. To date, the research focus has been mainly placed on ultrathin Pt monometallic or Pt-based bimetallic NWs [22]. The ultrathin Pt-trimetallic NWs, which possess the potential for further optimization of electronic structure and improvement of catalytic activity, have rarely been explored. Meanwhile, due to their structural fragility, it is also a grand challenge to unfold the full and optimized activity and stability of ultrathin NWs by traditional post-treatment, such as thermal annealing, thus bottlenecking the activity of this interesting catalytic system.

To address these issues, we herein report an ionic liquid (IL) (Fig. S1) conjugation strategy on ultrathin Pt-trimetallic NWs for greatly enhanced ORR performance. For this purpose, we first synthesize PtFeNi NWs with a mean diameter of only 2.2 nm *via* a facile wet-chemical approach and then conjugate the as-synthesized NW with the imidazolium-salt-based ILs (Fig. S2). In this system, 'conjugated' effect means the beneficial electronic interaction between inorganic nanomaterials and organic modifiers. In acidic media, the IL/PtFeNi NWs conjugate catalyst shows the impressive mass and specific activities of 2.83 A mg^{-1} and 3.24 mA cm^{-2}, respectively, much higher than those of non-IL-conjugated counterpart and commercial Pt/C. The IL conjugation is also beneficial for long-term stability due to the negligible activity decay after 30,000 potential cycles. To rationalize the role of IL conjugation for ORR electrocatalysis, we further carried out density functional theory (DFT) calculation, which indicates the dominant contribution of the strong electronic interaction between Pt and IL from IL conjugated PtFeNi NWs to the enhanced catalytic performance and the resultant weak oxygen binding energy relative to the non-IL-conjugated counterpart. Meanwhile, the ultrathin PtFeNi NWs/IL conjugate catalyst is highly general for enhancing the electrocatalytic activities of other important reactions such as methanol oxidation reaction (MOR) and H$_2$O$_2$ reduction reaction. Our findings offer a new opportunity for further optimization in electrocatalytic performance of fragile nanocrystals with atomic-level dimensionalities.

2. Experimental and theoretical section

2.1. Chemicals

Platinum (II) acetylacetonate (Pt(acac)$_2$, 97%), oleylamine (C$_{18}$H$_{35}$NH$_2$, OAm, 70%), iron(III) 2,4-pentanedionate (Fe(acac)$_3$, 99%), nickel(II) acetylacetonate (Ni(acac)$_2$, 99%), hexadecyl trimethyl ammonium Chloride (CTAC, 99%), molybdenum hexacarbonyl (Mo(CO)$_6$, 98%), 1-methylimidazole (99%), glucose and perchloric acid (HClO$_4$, 70%) were all purchased from Sigma-Aldrich. 3-Bromopropylamine hydrobromide (98%) was purchased from J&K Scientific Ltd. Nafion solution (5%) was purchased from Alfa Aesar. Cyclohexane (C$_6$H$_{12}$, 99.5%), methanol (CH$_3$OH, MeOH, 99.9%) and ethanol (C$_2$H$_5$OH, 99.7%) were purchased from Beijing Tongguang Fine Chemicals Company. Commercial Pt/C catalyst (20 wt %, 2–5 nm Pt nanoparticles on carbon black) was obtained from Johnson-Matthey Corp. All chemicals were used as received without further purification. The water (18 MΩ/cm) used in all experiment was prepared by passing through an ultra-pure purification system.

2.2. Materials synthesis

Synthesis of IL/PtFeNi NWs. In the typical synthesis of PtFeNi nanowires, 10 mg Pt(acac)$_2$, 1.4 mg Fe(acac)$_3$, 6 mg Ni(acac)$_2$, 40 mg Mo(CO)$_6$, 40 mg CTAC, 20 mg glucose and 10 mL oleylamine were added into 20 mL glass vial (Fig. S2). A clear homogeneous solution was obtained after sonicating for 1 h. Then, the vial was heated to 180 ℃ and kept at this temperature for 12 h. The obtained black colloidal product was collected by centrifugation (9000 rpm, 5 min), and washed with the mixture of cyclohexane and ethanol for three times. The final

precipitate was dispersed in cyclohexane for further use. 1-(3-Aminopropyl)-3-methylimidazolium bromide was prepared following the reference [23,24]. Finally, the combination of PtFeNi/C and ILs was conducted at a mass ratio of 1:1 by magnetic stirring overnight. The precipitate was collected by centrifugation and dried in the ambient environment.

2.3. Characterization

The TEM samples were prepared by dropping cyclohexane dispersed product onto carbon-coated copper transmission electron microscopy (TEM) grids using pipettes and dried under ambient condition. Low-magnification TEM was conducted on a FEI Tecnai-G2 T20. High-magnification transmission electron microscope (HRTEM) was conducted on a FEI Tecnai-G2 F30 at an accelerating voltage of 300 KV. XRD was conducted on an X'Pert-Pro X-ray powder diffractometer equipped with a Cu radiation source (λ = 0.15406 nm). The valence state was conducted by an X-ray photoelectron spectroscopy (XPS) (AXIS supra/ultra Kratos Analytical Ltd.). The elemental composition and concentration of PtFeNi/C catalyst were determined by the inductively coupled plasma mass spectrometer (Agilent SureCycler 8800 Gradient Cycler). Fourier-transform infrared (FT-IR) spectra were recorded with a Nicolet iS50 FT-IR spectrometer (Thermo Fisher Scientific, USA).

2.4. Electrochemical measurements

The as-prepared PtFeNi nanowires were deposited on carbon black (EC-300) before the electrochemical tests. The catalyst powder was dispersed in the solution containing isopropanol, water and Nafion (5%) (v: v: v = 1: 1: 0.016) to obtain a homogeneous ink. The rotating disk glassy carbon electrode (RDE, diameter: 5 mm, area: 0.196 cm^2) should be polished with Al$_2$O$_3$ powder and sonicated with water for 30 s. The ink was quantitatively dropped in the RDE to form a film work electrode. All the electrochemical tests were conducted in a traditional three-electrode system, the catalyst modified RDE, Ag/AgCl electrode and Pt foil were worked as working electrode, reference electrode and counter electrode, respectively. Cyclic voltammograms (CVs) were conducted in N$_2$-saturated 0.1 M HClO$_4$ at a scan rate of 50 mV/s. The ORR polarization curves were conducted in O$_2$-saturated 0.1 M HClO$_4$ at a scan rate of 20 mV/s and a rotation rate of 1600 rpm. The specific activity and mass activity were normalized by ECSA and the Pt mass loading, respectively. The durability tests were performed at O$_2$-saturated 0.1 M HClO$_4$ solution by applying the cyclic potential sweep between 0.6 and 1.0 V *versus* RHE at a sweep rate of 100 mV/s for 30,000 cycles. In the RRDE tests, the ring potential was set to 1.25 V *vs.* RHE. The MOR measurements were performed in N$_2$-saturated 0.1 M HClO$_4$ solution containing 0.1 M methanol at room temperature. The CVs for MOR were recorded between 0.1 and 1.2 V *versus* RHE at a scan rate of 50 mV/s. For the MOR stability tests, i-t test was recorded at a constant potential of 0.6 V *versus* RHE. For the measurements of H$_2$O$_2$ sensing, the CVs were performed in N$_2$-satureated 0.1 M PBS (pH 7.4) in the absence and the presence of H$_2$O$_2$ with different concentrations (0, 0.5, 1, 2, 3, 4, 5 mM). The measurements of i-t curves required operation of the electrode at a constant applied potential of 0.06 V.

2.5. Calculation setup

The PtFeNi NW structural model has been built based on the Pt (111) surface with four-layered thickness. We also implement the IL molecular structure into the PtFeNi model to simulate the IL-NW system, and the IL has been aligned as an array to mimic the local liquid environment nearby the PtFeNi surface.

We used the CASTEP code to perform the rotational invariant PBE + U calculations [25,26]. The Hubbard U parameter self-consistently determined for the pseudized Pt-5*d*, Fe-3d, and Ni-3d orbitals

by our new linear response method [27], which have been already successfully reflecting the electron-electron Coulomb potential for the semi-core orbitals should be considered when using DFT+U [27–32]. The geometry optimization used the Broyden-Fletcher-Goldfarb-Shannon (BFGS) algorithm through all calculations.

The plane-wave basis set cutoff energy is set to 750 eV. The ensemble DFT (EDFT) method of Marzari et al [33] is used for converging the transition metal contained electronic system. The supercell of PtFeNi surface model was built based on Pt-*fcc* (111) surface with total sizes of 144 atoms (*i.e.* $Pt_{132}Ni_8Fe_4$) and 4-layer thick. The vacuum thickness is set to be 15 Å. We only allow the top two layers to be varied

freely. The reciprocal space integration was performed using the mesh of $2 \times 2 \times 1$ [34]. The total energy is converged to less than 5.0×10^{-7} eV *per* atom. The Hellmann-Feynman forces on the atom were converged to less than 0.001 eV/Å.

The Pt, Ni, and Fe norm-conserving pseudopotentials are generated using the OPIUM code in the Kleinman-Bylander projector form [35], and the non-linear partial core correction [36] and a scalar relativistic averaging scheme [37] are used to treat the spin-orbital coupling effect. We choose non-linear core correction technique for correcting the Fe and Ni valence-core charge density overlapping. In particular, we treated the (5*d*, 6*s*, 6*p*) states as the valence states of Pt, and the (3*d*, 4*s*,
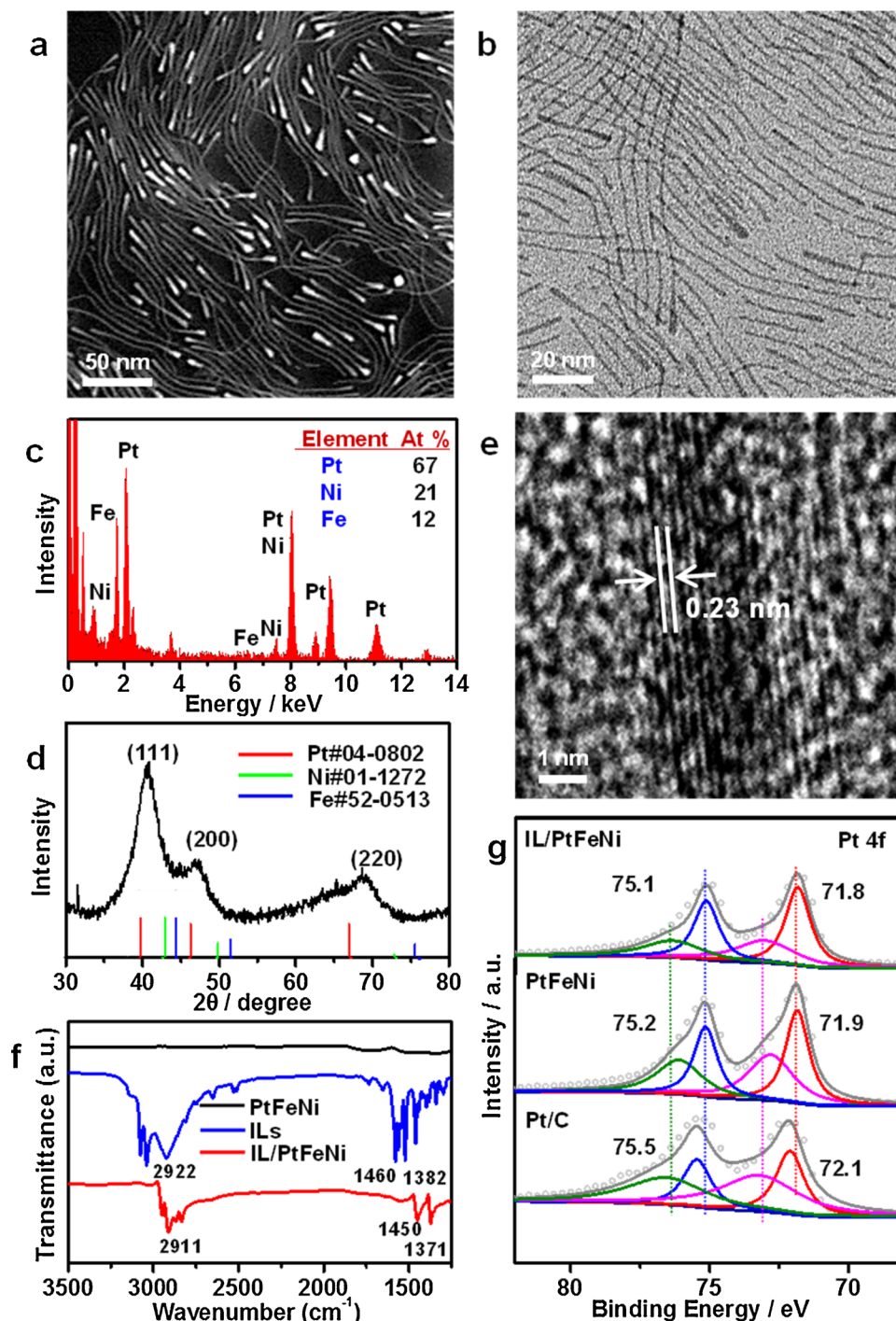

Fig. 1. Morphology and structure characterizations of 1D PtFeNi nanostructures. Representative a) STEM image, b) TEM image, c) EDS spectrum, d) PXRD patterns and e) HRTEM image of PtFeNi. f) FT-IR spectra of IL/PtFeNi NWs, ILs and PtFeNi. g) XPS patterns of IL/PtFeNi NWs, PtFeNi and Pt/C.

4p) configuration for Fe and Ni atoms. The RRKJ method is chosen for the optimization of the pseudopotentials [38].

For all of the electronic states calculations, we use the self-consistent determination for the U correction on the localized *d* orbitals to correct the on-site Coulomb energy of the electron spurious self-energy [39]. By that method, the Hubbard U parameters on the half-filled shell of $5d^9$ orbitals of Pt is self-consistently determined to be $U_d = 4.50$ eV, $U_d = 6.13$ eV for Fe, and $U_d = 4.27$ eV for Ni, respectively.

3. Results and discussion

The morphology and structure of as-prepared trimetallic PtFeNi NWs were characterized by transmission electron microscopy (TEM), highly-resolution TEM (HRTEM) and high-angle annular dark-field scanning TEM (HAADF-STEM). The representative low-magnification HAADF-STEM and TEM images reveal that 1-dimensional (1D) NWs with ultrathin characteristic dominate the as-synthesized products, approaching a yield of 100% (Fig. 1a, b). Based on the statistic of 200 samples, the average length and diameter of nanowires are determined to be 109 nm and 2.2 nm, respectively (Fig. S3). Energy-dispersive x-ray spectroscopy (EDS, Fig. 1c) reveals that the elemental composition of the nanowires follows a Pt/Ni/Fe atomic ratio of 67/21/12, in agreement with that determined from the inductively coupled plasma-atomic emission spectrometry (ICP-AES). The powder X-ray diffraction (PXRD) pattern of as-made nanowires shows several intense peaks centered at 40.8°, 47.2° and 69.2° (Fig. 1d), which can be readily assigned to the

(111), (200) and (220) diffraction planes of a face-centered cubic (*fcc*) phase. The corresponding peaks locate between those of Pt, Ni and Fe, confirming the yield of trimetallic solid-solution phase. HRTEM image of PtFeNi NWs further reveals their single crystalline nature, as verified by the continuous crystal lattice along the growing direction (Fig. 1e). The spacing distance is around 0.23 nm, being consistent with the (111) lattice plane of *fcc* PtFeNi alloy. The conjugation of ILs with the NWs is evident from the Fourier transform infrared spectroscopy (FTIR) spectrum (Fig. 1f), in which the characteristic bands of the C–H asymmetric stretching of methylene group at 2922 cm^{-1}, the C–H vibration of imidazole ring at 1460 cm^{-1} and the C–N vibration in ILs were shifted to 2911 cm^{-1}, 1450 cm^{-1} and 1371 cm^{-1} in IL/PtFeNi NWs, respectively. Collectively, the ILs surface-modified ultrathin PtFeNi NWs have been successfully synthesized (Fig. S2).

To shed light on the growth mechanism of ultrathin Pt-based trimetallic NWs, we further characterized the products from various representative reaction stages by TEM (Fig. S4). At the very beginning of the synthesis (10 min), the products are dominated with ultrathin nanorods, the length of which ranges from 2.2 nm to 4.3 nm. As the reaction proceeded to 30 min, the length of NWs gradually grew to ~17 nm, while the thickness remains 2.2 nm, indicating the anisotropic growing phenomenon. Well-defined and high-quality ultrathin NWs were readily obtained after 5 h reaction. Notably, during all three periods, we do not observe the presence of small nanocrystals, indicating that the nucleation of metallic precursor occurs heterogeneously on the surface of 1-dimensional nanocrystals [40]. Therefore,
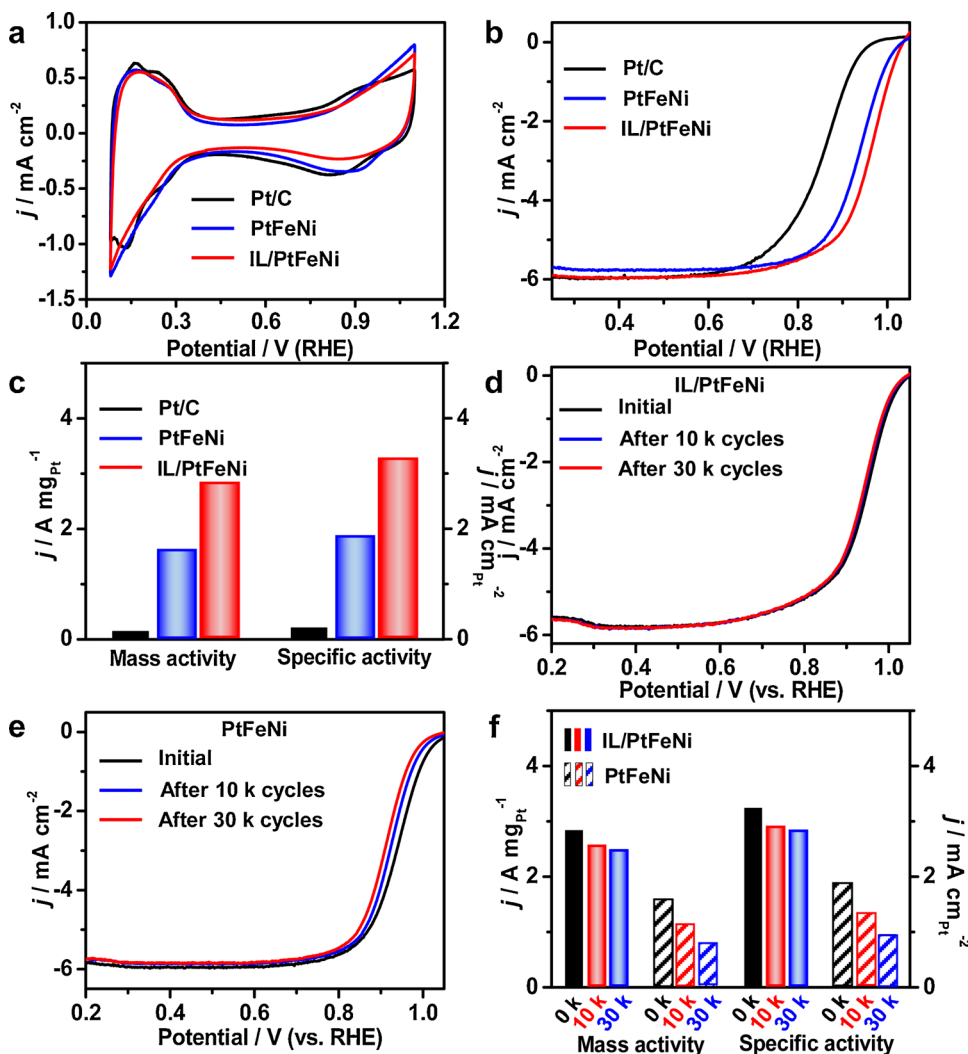

Fig. 2. Electrocatalytic performance of IL/PtFeNi NWs, PtFeNi and commercial Pt/C. a) CVs were recorded at room temperature in 0.1 M HClO₄ solution. b) ORR polarization curves were recorded at room temperature in an O₂-saturated 0.1 M HClO₄ aqueous solution at a sweep rate of 20 mV/s and a rotation rate of 1600 rpm. c) Comparison on the mass activities and specific activities. d–f) Electrocatalytic durability of IL/PtFeNi NWs, PtFeNi and commercial Pt/C. ORR polarization curves of d) IL/PtFeNi NWs and e) PtFeNi before and after 10 k, 30 k potential cycles between 0.6 and 1.0 V *versus* RHE. The ORR polarization curves were recorded at room temperature in an O₂-saturated 0.1 M HClO₄ aqueous solution. f) The changes in mass and specific activities of IL/PtFeNi NWs and PtFeNi before and after different potential cycles.

we propose that the formation of ultrathin 1D nanowires proceeds through seed-mediated growth in our system, rather than oriented attachment of small nanocrystals [41,42]. The absence of twin boundary (indicating the attachment interface) throughout the NWs from HRTEM further verifies out the proposal (Fig. S4).

The cyclic voltammograms (CVs) of IL/PtFeNi NWs, PtFeNi NWs, and commercial Pt/C were first recorded in N_2-saturated 0.1 M $HClO_4$ solution to probe the surface properties of these catalysts. As shown in Fig. 2a, all three samples display well-defined electrochemical characteristics of Pt electrode: the hydrogen under-potential adsorption/desorption ($H_{upa/upd}$) peaks and oxidation/reduction redox peaks. The electrochemically active surface area (ECSA) of each catalyst was calculated from the correspondingly integrated area of H_{upd} peak (see SI for details). The IL/PtFeNi NWs displays an outstandingly high ECSA of 87.50 m^2/g, higher than those of PtFeNi NWs (84.66 m^2/g) and commercial Pt/C (72.29 m^2/g) (Table S1). The onset potentials for hydroxide adsorption of IL/PtFeNi NWs and PtFeNi NWs shift to higher potential significantly relative to that of commercial Pt/C, indicative of decreased oxygen adsorptive strength on these two trimetallic catalysts. Such phenomenon has also been widely observed on PtM (M denote as other transition metals) alloy catalysts, which can be ascribed to the electronic tuning of Pt by M, *i.e.*, the so-called ligand effect [43,44]. Notably, after IL conjugation, the hydroxyl adsorption on IL/PtFeNi NWs was further depressed in comparison with the non-conjugation counterpart, as verified from the position and intensity of either oxidation or reduction peak. This interesting observation indicates the IL can also tune the electronic structure of Pt, as supported by the XPS characterization (Fig. 1g and Fig. S5).

Fig. 2b compares the ORR polarization curves of various catalysts recorded at room temperature at a sweep rate of 20 mV/s and a rotation rate of 1600 rpm in O_2-saturated 0.1 M $HClO_4$. The mass and specific activities of IL/PtFeNi NWs catalyst reach 2.83 A mg^{-1} and 3.24 mA cm^{-2}, respectively, with impressive improvement factors of 1.72 over PtFeNi NWs, 15.5 over Pt/C catalyst, respectively (Fig. 2c), clearly indicating the promoting role of IL conjugation to the ORR on Pt surface. Fig. 2d–f shows the ORR polarization curves of different catalysts after different long-term potential cycles. The changes in both mass and specific activities of different catalysts were calculated. We found that IL/PtFeNi NWs shows the best stability with a small portion decrease in their initial mass and specific activity in all the investigated catalysts (Fig. 2f). The mass and specific activities of IL/PtFeNi NWs were still as high as 2.49 A mg^{-1} and 2.84 mA cm^{-2}, respectively, after 30,000 cycles, demonstrating the capability of IL coverage in preserving the initial high catalytic activity. In contrast, the ultrathin PtFeNi NWs and commercial Pt/C catalyst have bigger mass activity (Fig. S6 & Fig. 2e,f). The improved catalytic stability of IL/PtFeNi NWs is mainly due to the minimization of transition metal dissolution during the long-term operation, as confirmed by the TEM-EDS (Fig. S7a, b) and XPS (Fig. S8). To further investigate the reaction kinetics of the catalysts during the ORR process, the electron-transfer number *n* of IL/PtFeNi NWs during the ORR was also calculated based on the ring-rotated disk electrode (RRDE) results (Fig. S9a, b). It can be seen that the *n* values of the IL/PtFeNi NWs remain close to 4, indicating a four-electron pathway reduction of O_2 on the IL/PtFeNi NWs.

To reveal the ORR promoting mechanism of IL conjugation, we further carried out DFT calculations and stimulated ORR on both PtFeNi and IL/PtFeNi systems. First, the HOMO-LUMO orbital distribution is exhibited on the native Pt-*fcc* (111) surface to find the character of periodic alternation for the electronic occupation near the Fermi level (E_F) (Fig. 3a). The surface electronics of the PtFeNi (111) system differ from those of the Pt-*fcc* (111), showing almost electron-richer modulated distribution on the surface (Fig. 3b). In the IL/PtFeNi system, the surface electronic filled-states have almost shielded the empty states with the effect of the IL layer coverage (Fig. 3c). The roles of Fe and Ni-sites on the PtFeNi surface have also been explored. They both perform the effective electronic modulations in a long-range order
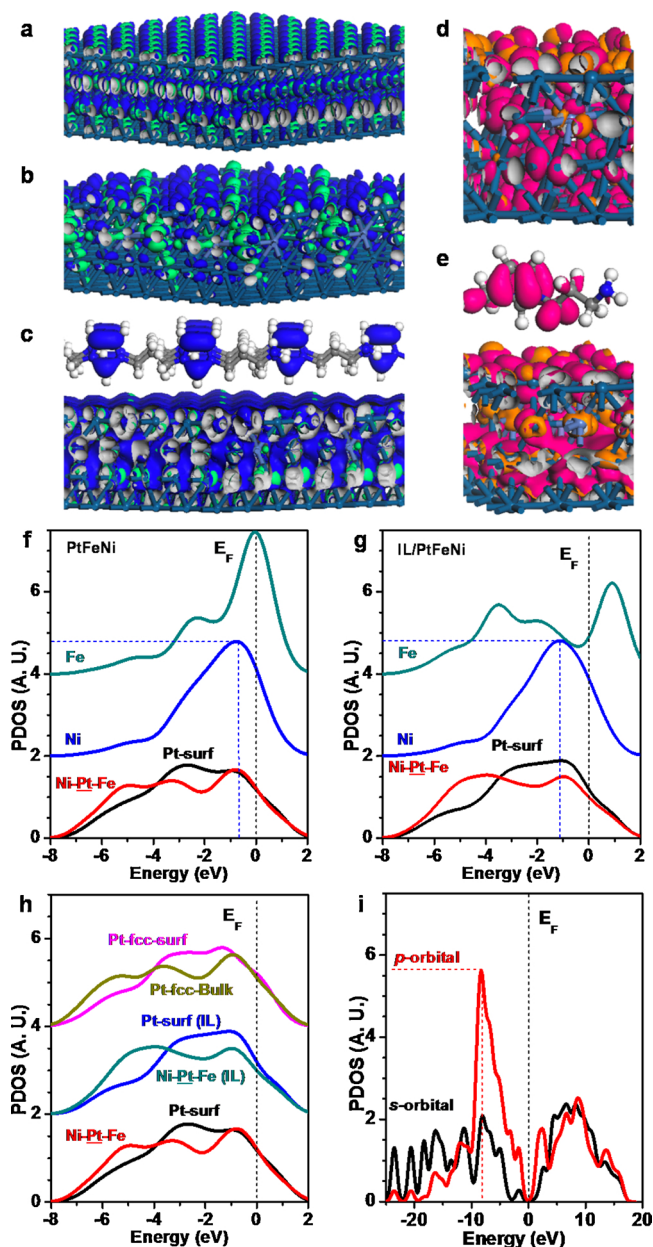

Fig. 3. a–c) The atomic structural configuration and the local orbital 3D contour plots of the HOMO and LUMO for Pt-*fcc* (111), PtFeNi (111), and IL/PtFeNi NWs (111) systems, are shown respectively. d–e) Local orbital 3D contour plots of the d-orbital at the d-band centers of surface Fe and Ni-sites in the PtFeNi (111) and IL/PtFeNi NWs (111) systems, are shown, respectively. f) The PDOSs of the d-bands for inner Ni-Pt-Fe site (nearest neighboring Fe and Ni sites), Fe-site, and Ni-site on the PtFeNi (111) system. g) The PDOSs of the d-bands for inner Ni-Pt-Fe site (nearest neighboring Fe and Ni sites), Fe-site, and Ni-site on the IL/PtFeNi NWs (111) system. h) The PDOSs benchmarks for the Pt-5d-bands from three different surface systems, Pt-*fcc* (111), PtFeNi (111) and IL/PtFeNi NWs (111), respectively. i) The PDOSs of the sp orbital components of the IL molecule system.

(Fig. 3d). With the ILs coverage, both Fe and Ni 3d orbitals are more delocalized with a larger cross-section of potential orbital overlapping probabilities on the surface, showing synergetic effect with ILs (Fig. 3e).

The surface electronic modifications have been also reflected through the projected partial density of states (PDOSs) calculations. On the PtFeNi surface (Fig. 3f), the d-band center for the inner layered Pt connecting by nearest neighboring Ni and Fe site (*i.e.* Ni-Pt-Fe) is about E_V, -3.0 eV where the $E_V = 0$ for E_F, while the top surface Pt-site has a higher center of E_V, -2.5 eV. The Ni-3d-band center locates at the level

of E_V, -1.5 eV. The e_g-t_{2g} splitting effect for the Fe-3d orbital has been absent potentially due to the disturbance of the surface local crystal-field. The d-band center of Fe is E_V, -0.7 eV and all the 3d-electronic-states merge at the E_F level.

In the IL/PtFeNi system, the surface electronic structures have been evidently modified (Fig. 3g). The dominant 5d-orbital peak of the inner Ni-Pt-Fe site has been suppressed with d-band center of E_V, -3.5 eV, while the top Pt-site shows the center of E_V, -1.7 eV with higher charge-transfer activities, indicating a better initial O-adsorption on the Pt-exposed-surface within ILs. The Fe-3d-band clearly shows the e_g-t_{2g} splitting, implying an effective crystal-field effect. It indicates a well-preserved local field shielded by the ILs environment. The e_g state that staying slightly above E_F shows substantial less electronic occupation than the t_{2g} level, and the t_{2g} level peak centers at E_V, -3.1 eV. On the other hand, the IL shielding effect also induced the Ni-3d band center to move slightly higher at E_V, -1.4 eV, showing an electronic depletion towards nearby ions. By comparing in detail (Fig. 3h), we confirm that the electronic activities of Pt sites can be still evidently modulated by the Ni and Fe sites even within ILs regardless the inner or topmost surface regions, and the IL does not influence those d-orbitals with totally mismatched band-alignment (Fig. 3i). From the view on the electronic orbital occupation, the *electronic chemical potential* is contributed by the corresponding on-site orbital occupations. Note the $\delta E/\delta n$ usually represents the functional of the on-site surface *chemical potential field* distribution [45–47], where the E represents the total energies of the targeted surface system, and the n is the surface on-site electronic orbital occupations. We import the *variation* symbol (δ) to represent the complexity of the surface catalytic system controlled by many uncertain variables and parameters. Thus, we proposed that the

IL environment promotes the surface electronic activity to be more evenly as well as the distributed "*chemical-field*".

The free energetic pathways for acidic four-electron ORR based on Pt, PtFeNi and IL/PtFeNi systems have been shown and compared, respectively (Fig. S10a). Among these pathways, we mainly compare and discuss the electrode potentials of U = 0 and U = 1.23 V for different up- and down-hill behaviors. In these pathways, we find that the rate-determining steps are aligned and all appear at the last reduction step, [*OH + H] → H_2O*, with a reaction barrier of 0.4~0.9 eV. In the environment of U = 0, Pt (111) shows nearly downhill process except the last reduction step of [*OH + H_2O + H^+ + e^-] has shown a very minor uphill barrier with the energy level of 0.85 eV reference to the H_2O level (ΔG = 0 eV). Overall, the initial adsorption for the Pt (111) (3.02 eV) shows better initial adsorption than the PtFeNi (4.13) but still energetically higher than the IL/PtFeNi (1.55 eV). We summarize the overpotentials from the difference between the final reduction step and H_2O-level, which are 0.85 V, 0.49 V, and 0.40 V for Pt-*fcc*, PtFeNi, and IL/PtFeNi systems, respectively. These potentials are in a good agreement with our experimental measurement, and the value for Pt system also follows in consistent range with the one obtained by Nøskov et al. [48] based on the two-electron ORR pathway. Therefore, the IL/PtFeNi energetically favors ORR catalysis at the overpotential substantially lower than the Pt system (~0.85 V *vs.* standard hydrogen electrode). From the local structures (Fig. S10b), the initial O−O adsorption and [*O═O−H] stabilization are shown on the Pt-exposed surface within IL environment. The higher catalytic activities arise from the enhanced charge transfer between Pt-(O═O) and Pt-(O═O═H) species. The flexible coverage provides the optimally shielding to enhanced the Pt-(O═O) binding instead of strong Pt-O bond, indicating a well-preserved
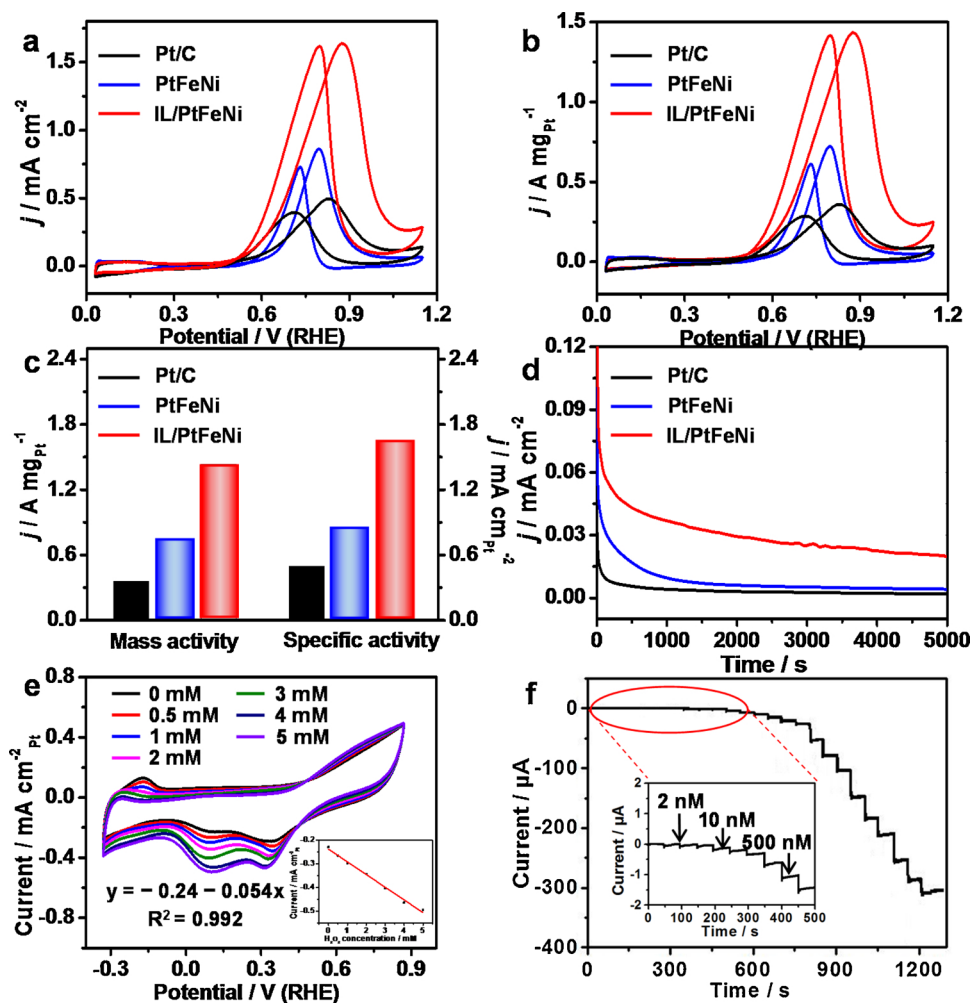

Fig. 4. a–d) MOR Performance. a) ECSA- and b) Pt mass-normalized CVs of IL/PtFeNi NWs, PtFeNi and commercial Pt/C recorded in 0.1 M $HClO_4$ solution containing 0.1 M CH_3OH. c) Histogram of specific activity and mass activity. d) i-t test of IL/PtFeNi NWs, PtFeNi and commercial Pt/C, recorded at a constant potential of 0.6 V *vs* RHE. e) CVs of IL/PtFeNi NWs in N_2-saturated 0.1 M PBS (pH 7.4) in the absence and H_2O_2 with different concentrations (0, 0.5, 1, 2, 3, 4, 5 mM). The *inset* shows the calibration curve of the amperometric response to the concentration of H_2O_2 from 0 nM to 5 mM. f) Amperometric responses of IL/PtFeNi NWs modified GC electrode to the successive addition of H_2O_2 in PBS an applied potential of 0.06 V. The *inset* shows a close look of the red oval region with the H_2O_2 concentration from 0 to 1.54 μM. (For interpretation of the references to colour in this figure legend, the reader is referred to the web version of this article).

four-electron ORR path guaranteed. As is known, the over-binding of Pt-O usually produces the unexpected earlier O—O bond cleavage to redirect into inefficient two-electron reduction pathway. With these synergetic effects, the efficiency of adsorption/desorption steps has been increased with barrier free. By discussing the trends of electronics and energetics, we further confirm that the IL/PtFeNi system has a substantially high electrocatalytic activity, which activates the high ORR energetic performance simultaneously.

After the investigation of the exceptional performance of IL/PtFeNi from both experimental characterizations and theoretical explorations, the feasibility of such electrocatalyst in other general electrocatalysis is also crucial. Thus, we also verified its performance in methanol oxidation reaction (MOR) and H_2O_2 detection. As shown in Fig. 4a, b, we evaluated the catalytic activity of various catalysts towards the methanol oxidation reaction (MOR). The peak potential of MOR on IL/PtFeNi NWs positively shifted by 60 mV compared with that of the PtFeNi NWs, indicating that ILs plays an important role in accelerating the electron transfer. The peak current density of IL/PtFeNi NWs was 1.9 and 4.0 times higher than that of PtFeNi NWs and commercial Pt/C, respectively (Fig. 4c, Table S2). After chronoamperometric recording for 5000 s, the IL/PtFeNi NWs maintained significantly larger current density than other two controls, suggesting its excellent durability towards the MOR (Fig. 4d).

We further evaluated the capability of IL/PtFeNi NWs in electrodetection of H_2O_2 molecules. To verify the sensitivity of IL/PtFeNi NWs toward H_2O_2 reduction, the CVs were recorded in different H_2O_2 concentrations range from 0 to 5 mM (Fig. 4e). Upon stepwise adding the amounts of H_2O_2, both the anodic oxidation current and catholic oxidation current increased. A good linear relationship was observed when plotting the peak reduction current as a function of the H_2O_2 concentration, indicating the fairly good response. A typical current-time (i-t) curve for H_2O_2 detection is presented in Fig. 4**f**. The result showed that with the injection of H_2O_2, the current on IL/PtFeNi NWs steadily increases. Meanwhile, the steady-state current can be achieved within several seconds, demonstrating its rapid electrochemical response to H_2O_2. The amplified image of 0–500 s of the sensing curve is presented in the inset of Fig. 4**f**, from which we observed the IL/PtFeNi NWs took steep and stable amperometric responses after each small injection of H_2O_2. The lowest detectable concentration is 2 nM, which is sensitive enough for applications such as detecting H_2O_2 in the biological system.

4. Conclusions

In conclusion, utilizing the ultrathin Pt-based trimetallic nanowires as the model catalyst, we demonstrated the superior ORR activity originated from the surface conjugation of IL. Theoretical calculations reveal that the enhanced electrocatalytic activity is attributed to the optimized charge transfer between the conjugated Pt and adsorbed species at lower potentials. The flexible coverage provided optimally shielding to enhance the Pt-(O═O) binding instead of strong Pt-O bond, thus giving rise to a well-preserved four-electron ORR path by efficiently blocking the two-electron path. The IL/PtFeNi NWs conjugate catalyst also exhibited the enhanced activity towards the MOR, along with promoted performance for the H_2O_2 sensing. This study opens a new avenue to further boost the electrocatalytic performance of fragile *yet* promising Pt-based nanocrystals *via* rational interfacial engineering.

Acknowledgements

Appendix A. Supplementary data

Supplementary material related to this article can be found, in the online version, at doi:https://doi.org/10.1016/j.apcatb.2019.117828.

References

[1] A. Kongkanand, M.F. Mathias, J. Phys. Chem. Lett. 7 (2016) 1127–1137.
[2] O. Gröger, H.A. Gasteiger, J.P. Suchsland, J. Electrochem. Soc. 162 (2015) A2605–A2622.
[3] S. Chu, A. Majumdar, Nature 488 (2012) 294–303.
[4] Z.W. Seh, J. Kibsgaard, C.F. Dickens, I.B. Chorkendorff, J.K. Nørskov, T.F. Jaramillo, Science 355 (2017) eaad4998.
[5] M. Luo, Y. Sun, L. Wang, S. Guo, Adv. Energy Mater. 7 (2017) 1602073.
[6] H.A. Gasteiger, S.S. Kocha, B. Sompalli, F.T. Wagner, Appl. Catal. B 56 (2005) 9–35.
[7] M. Shao, Q. Chang, J.P. Dodelet, R. Chenitz, Chem. Rev. 116 (2016) 3594–3657.
[8] H. Yang, Angew. Chem. Int. Ed. 50 (2011) 2674–2676.
[9] M.K. Debe, Nature 486 (2012) 43–51.
[10] Y. Jiao, Y. Zheng, M. Jaroniec, S.Z. Qiao, Chem. Soc. Rev. 44 (2015) 2060–2086.
[11] Y.J. Wang, N. Zhao, B. Fang, H. Li, X.T. Bi, Chem. Rev. 115 (2015) 3433–3467.
[12] J.K. Nørskov, T. Bligaard, J. Rossmeisl, C.H. Christensen, Nat. Chem. 1 (2009) 37–46.
[13] I.E.L. Stephens, J. Rossmeisl, I. Chorkendorff, Science 354 (2016) 1378–1379.
[14] M. Luo, S. Guo, Nat. Rev. Mater. 2 (2017) 17059.
[15] V.R. Stamenkovic, D. Strmcnik, P.P. Lopes, N.M. Markovic, Nat. Mater. 16 (2016) 57–69.
[16] M. Luo, Y. Sun, X. Zhang, Y. Qin, M. Li, Y. Li, C. Li, Y. Yang, L. Wang, P. Gao, G. Li, S. Guo, Adv. Mater. 30 (2018) 1705515.
[17] M. Li, Z. Zhao, T. Cheng, A. Fortunelli, C.Y. Chen, R. Yu, Q. Zhang, L. Gu, B.V. Merinov, Z. Lin, E. Zhu, T. Yu, Q. Jia, J. Guo, L. Zhang, W.A. Goddard III, Y. Huang, X. Duan, Science 354 (2016) 1414–1419.
[18] M. Escudero-Escribano, P. Malacrida, M.H. Hansen, U.G. Vej-Hansen, A. Velázquez-Palenzuela, V. Tripkovic, J. Schiotz, J. Rossmeisl, I.E. Stephens, I. Chorkendorff, Science 352 (2016) 73–76.
[19] S. Guo, S. Zhang, S. Sun, Angew. Chem. Int. Ed. 52 (2013) 8526–8544.
[20] K. Jiang, D. Zhao, S. Guo, X. Zhang, X. Zhu, J. Guo, G. Lu, X. Huang, Sci. Adv. 3 (2017) e1601705.
[21] Y. Sun, M. Luo, Y. Qin, S. Zhu, Y. Li, N. Xu, X. Meng, Q. Ren, L. Wang, S. Guo, ACS Appl. Mater. Interfaces 9 (2017) 34715–34721.
[22] S. Guo, D. Li, H. Zhu, S. Zhang, N.M. Markovic, V.R. Stamenkovic, S. Sun, Angew. Chem. 125 (2013) 3549–3552.
[23] Y. Zhang, Y. Shen, J. Yuan, D. Han, Z. Wang, Q. Zhang, L. Niu, Angew. Chem. 118 (2006) 5999–6002.
[24] S. Guo, S. Dong, E. Wang, Adv. Mater. 22 (2010) 1269–1272.
[25] S.J. Clark, M.D. Segall, C.J. Pickard, P.J. Hasnip, M.I. Probert, K. Refson, M.C. Payne, Zeitschrift Fur Kristallographie-Crystalline Materials 220 (2005) 567–570.
[26] V.I. Anisimov, F. Aryasetiawan, A.I. Lichtenstein, J. Phys. Condens. Matter 9 (1997) 767–808.
[27] B. Huang, J. Comput. Chem. 37 (2016) 825–835.
[28] B. Huang, R. Gillen, J. Robertson, J. Phys. Chem. C 118 (2014) 24248–24256.
[29] B. Huang, Philos. Mag. 94 (2014) 3052–3071.
[30] B. Huang, Solid State Commun. 230 (2016) 49–53.
[31] B. Huang, Solid State Commun. 34 (2016) 237–238.
[32] B. Huang, Phys. Chem. Chem. Phys. 18 (2016) 13564–13582.
[33] N. Marzari, D. Vanderbilt, M.C. Payne, Phys. Rev. Lett. 79 (1997) 1337–1340.
[34] M.I.J. Probert, M.C. Payne, Phys. Rev. B 67 (2003) 075204.
[35] L. Kleinman, D.M. Bylander, Phys. Rev. Lett. 48 (1982) 1425–1428.
[36] S.G. Louie, S. Froyen, M.L. Cohen, Phys. Rev. B 26 (1982) 1738–1742.
[37] I. Grinberg, N.J. Ramer, A.M. Rappe, Phys. Rev. B 62 (2000) 2311–2314.
[38] A.M. Rappe, K.M. Rabe, E. Kaxiras, J.D. Joannopoulos, Phys. Rev. B 41 (1990) 1227–1230.
[39] J.K. Nørskov, J. Rossmeisl, A. Logadottir, L.R.K.J. Lindqvist, J.R. Kitchin, T. Bligaard, H. Jonsson, J. Phys. Chem. B 108 (2004) 17886–17892.
[40] B. Lim, M. Jiang, T. Yu, P.H. Camargo, Y. Xia, Nano Res. 3 (2010) 69–80.
[41] K.D. Gilroy, A. Ruditskiy, H.C. Peng, D. Qin, Y. Xia, Chem. Rev. 116 (2016) 10414–10472.
[42] B. Lim, Y. Xia, Angew. Chem. Int. Ed. 50 (2011) 76–85.
[43] V.R. Stamenkovic, B. Fowler, B.S. Mun, G. Wang, P.N. Ross, C.A. Lucas, N.M. Marković, Science 315 (2007) 493–497.
[44] V. Stamenkovic, B.S. Mun, K.J. Mayrhofer, P.N. Ross, N.M. Markovic, J. Rossmeisl, J. Greeley, J.K. Nørskov, Angew. Chem. 118 (2006) 2963–2967.
[45] J.P. Perdew, A. Zunger, Phys. Rev. B 23 (1981) 5048–5079.
[46] R.G. Parr, R.A. Donnelly, M. Levy, W.E. Palke, J. Chem. Phys. 68 (1978) 3801–3807.
[47] B. Huang, Phys. Chem. Chem. Phys. 19 (2017) 8008–8025.
[48] J.K. Nørskov, J. Rossmeisl, A. Logadottir, L.R.K.J. Lindqvist, J.R. Kitchin, T. Bligaard, H. Jonsson, J. Phys. Chem. B 108 (2004) 17886–17892.